Available online at www.sciencedirect.com

ScienceDirect

IFAC PapersOnLine 55-26 (2022) 193–199

Data-driven control-oriented reduced order modeling for open channel flows [⋆]

Henry Baumann [*] Alexander Schaum [*] Thomas Meurer [*]

[*] *Automation and Control Group, Department of Electrical and Information Engineering, Kiel University, Kaiserstr. 2, 24143 Kiel, Germany (e-mail: {heba,alsc,tm}@tf.uni-kiel.de).*

Abstract: Model order reduction can be used for efficient simulation of complex systems. Data-based system identification approaches using neuronal networks or Dynamic Mode Decomposition enable us to extract characteristic properties of the system dynamics in order to reduce them to a low-dimensional space. There the temporal propagation can be described with significantly less computational effort. Both approaches are applied to the boundary actuated St. Venant equations, to obtain control-oriented reduced order models, which try to capture the dynamics of open channel flows for a wide range of input signals. It is investigated whether these models can be used for efficient simulation and how accurately they reconstruct the dynamic behavior of the water depth and velocity of an open channel.

Keywords: Model order reduction, Autoencoder, EDMDc, St. Venant equations, Koopman theory.

1. INTRODUCTION

Modeling and automatic control of water networks is becoming increasingly important, not least due to global warming. Water networks include, e.g., irrigation, rainwater and sewer networks. Hydrodynamic modeling tools like the open source Storm Water Management Model (SWMM) can be used for modeling and simulation of such systems. The individual components of a water network can be considered and modeled separately. Besides catchment areas, retention basins and other facilities, the channel reaches are central to describe the flow of the water in a network.

A single channel can be described in detail using the nonlinear partial differential equations (PDEs) of Saint-Venant (1871), which can be derived from the Navier-Stokes equations. Usually the gate opening or the wire position and thus the discharge at the boundaries of a channel forms the input of the system. The methods to solve such a control problem can be divided into early lumping (i.e., approximation based) and late lumping (i.e., PDE based) approaches. With respect to late lumping Diagne et al. (2015); Rabbani et al. (2010) used a linearized model to design a backstepping or flatness based controller for irrigation channels. These approaches lead typically to infinite-dimensional feedback controllers that need to be discretized for implementation purposes. With regard to early lumping the design of a control law is done based on a discretized model, which has been presented by Xu et al. (2012); Zeng et al. (2020). Optionally, the flow of open channels can be described using simplifications of the St. Venant equations or conceptual models. Examples include the Muskingum and Integrator Delay Model. These models and corresponding control laws can be computed significantly faster compared to using a discretized model, but normally do not contain information about the water level and the discharge of the whole channel. A comprehensive review for modeling and control of irrigation channels is given in Conde et al. (2021). The aforementioned hydrodynamic simulation tools such as SWMM are capable for accurate simulation, but due to their complexity, these approaches are less suitable for computationally intensive optimal control. For this purpose, a reduced order model (ROM) can be used, which reduces the model order while preserving all relevant dynamics.

One approach that seems suitable to describe the dynamic behavior of the entire water surface is Koopman operator-based model order reduction (MOR). The main idea is to identify some characteristic properties of the channel dynamics and how they evolve in time. Recently data-driven Koopman operator identification techniques like Dynamic Mode Decomposition (DMD) and autoencoders (AEs) have shown to be useful tools for MOR. Brunton and Kutz (2019) give an extensive overview of data-based modeling. The basic methods for system identification have been extended by Proctor et al. (2016b,a) to consider control inputs. Hence, complex high-dimensional systems can be simulated and even controlled using information from the low-dimensional subspace. Applications are found in various areas such as fluid dynamics, neuroscience, epidemiology among others (Maksakov and Palis, 2021; Brunton et al., 2021; Arbabi et al., 2018).

DMD has been used to identify coherent structures of the 2D St. Venant equations for one specific scenario (Ahmed et al., 2020; Bistrian and Navon, 2015). Maulik et al. (2021) addresses this similarly using convolutional AEs. However, the focus in these paper was on the reconstruc-

[⋆] The first author (Henry Baumann) is supported by the NEPTUN project. NEPTUN is financed by Interreg Deutschland-Danmark with means from the European Regional Development Fund.

10.1016/j.ifacol.2022.10.399

tion and prediction of the high-dimensional system for a specific scenario rather than the identification of a control-oriented model. Such a model should cover the dynamics broadly in order to enable an exact simulation with different input signals. Further it should noted that MOR techniques usually do not consider conservation properties, which hinders the creation of a ROM with input. To the best of the authors knowledge no investigations on control-oriented reduced order modeling of channel reaches using Koopman operator theory has been reported so far.

In the following a data-driven control-oriented model is determined, which enables a reconstruction of the channel quantities. Thereby, the aforementioned issue of preserving conservation properties is addressed by appropriate preprocessing. A ROM is obtained from preprocessed simulation data of the discretized St. Venant equations using DMD with control and AEs. Note that a controller is not designed within the scope of this paper. First the detailed model of water in a single channel and its numerical solution are described in Section 2. An overview of Koopman operator theory and data-driven system identification using DMD and AE approaches is given in Section 3. Thereupon, in Section 4, the preprocessing is shown, before the presented MOR approaches are applied and simulatively evaluated in 5. Finally, Section 6 concludes this paper with a summary and remarks for future investigations.

2. MODELING OF OPEN CHANNEL REACHES

The fluid in open channels can be modeled using the St. Venant equations which is a set of coupled nonlinear PDEs. Inside the spatial domain $x \in (0, L)$ of length L, the wetted area A and the discharge Q at time $t > 0$ can be described using the mass balance and momentum equation

$$\partial_t A + \partial_x Q = 0 \tag{1a}$$

$$\partial_t Q + \partial_x \left(\frac{Q^2}{A}\right) + gA(\partial_x h + S_f - S_0) = 0 \tag{1b}$$

with the initial conditions

$$A(x,0) = A_0, \qquad x \in [0,L], \tag{1c}$$

$$Q(x,0) = Q_0, \qquad x \in [0,L]. \tag{1d}$$

The upstream and downstream discharge determine the boundary conditions

$$Q(0,t) = Q_{\mathrm{up}}(t), \qquad t \in \mathbb{R}_0^+, \tag{1e}$$

$$Q(L,t) = Q_{\mathrm{down}}(t), \qquad t \in \mathbb{R}_0^+, \tag{1f}$$

which form the system inputs. The gravitational acceleration and the bed slope are denoted as g and S_0, respectively. For the friction slope S_f the relation

$$S_f = n_M^2 \frac{Q|Q|}{A^2 R^{4/3}} \tag{2}$$

of Manning-Strickler can be used. There the friction coefficient n_M, which is also referred to as Manning's coefficient, can be used to calibrate the model to the friction of the reach. Further R denotes the hydraulic radius, which varies with the water depth $h > 0$ and cross-section of the channel. An open channel with a trapezoidal cross-section is shown schematically in Figure 1. From this it can be seen that the wetted area of a trapezoidal channel is

$$A(h) = h(B + mh) \tag{3}$$

with the bed width B and the bank slope m, which are assumed to be constant along the channel.

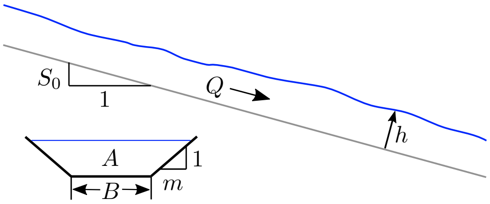

Fig. 1. Schematic representation of an open channel with trapezoidal cross-section.

Since no analytical solution has been found for the governing equations, the PDEs have to be solved numerically. As the St. Venant equations are hyperbolic PDEs, conservation properties have to be taken into account when choosing a numerical scheme. Therefore different approaches have been presented including the implicit Preismann scheme or the semi-implicit scheme of Casulli (1990), which is used in this work. It has been preferred over the method of characteristics, because it is more suitable for complex channel cross-sections and for accurate mass conservation. Optionally finite volume or finite element approaches could be used, therefore see, e.g., Benkhaldoun and Seaïd (2010) and Utnes (1990).

The semi-implicit scheme of Casulli (1990) is based on the (v, h)-form of the St. Venant equations, which can be obtained from (1a) and (1b) after applying the chain rule and using the relationship

$$Q = vA(h) \tag{4}$$

with velocity v. The resulting (v, h)-form reads

$$\partial_t h + \frac{1}{\partial_h A(h)} \partial_x (vA(h)) = 0, \tag{5a}$$

$$\partial_t v + v\partial_x v + g\left(\partial_x h - S_0 + n_M^2 \frac{v|v|}{R(h)^{4/3}}\right) = 0, \tag{5b}$$

with the initial and boundary conditions

$$h(x,0) = -\frac{B}{2m} + \sqrt{\left(\frac{B}{2m}\right)^2 + \frac{A_0}{m}}, \qquad x \in [0,L], \tag{5c}$$

$$v(x,0) = \frac{Q_0}{A_0}, \qquad x \in [0,L], \tag{5d}$$

$$v(0,t)A(h(0,t)) = Q_{\mathrm{up}}(t), \qquad t \in \mathbb{R}_0^+, \tag{5e}$$

$$v(L,t)A(h(L,t)) = Q_{\mathrm{down}}(t), \qquad t \in \mathbb{R}_0^+. \tag{5f}$$

Introducing the spatial discretisation scheme shown in Figure 2, the domain is divided into N equidistant sections of width Δx. The water depth $\boldsymbol{h} = [h_1, \dots, h_N]^T$ is computed on the center of the sections, while the velocities $\boldsymbol{v} = [v_{1/2}, \dots, v_{N+1/2}]^T$ are computed on their edges. Based on this notation and the staggered grid, the finite difference scheme applied to (5a) yields

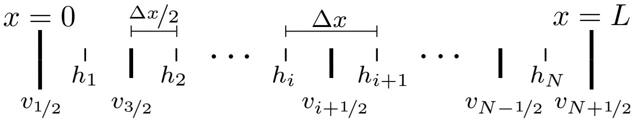

Fig. 2. Schematic representation of the discretisation grid.

$$\frac{h_i^{\kappa+1} - h_i^\kappa}{\Delta t} = -\frac{1}{(\partial_h A)_i^\kappa} \frac{v_{i+1/2}^{\kappa+1} A_{i+1/2}^\kappa - v_{i-1/2}^{\kappa+1} A_{i-1/2}^\kappa}{\Delta x}, \tag{6}$$

where κ and Δt denote the time step and sample time, respectively. For the first and last section of the domain the boundary conditions (5e) and (5f) can be imposed through $v^{\kappa+1}_{1/2}A^{\kappa}_{1/2} = Q^{\kappa+1}_{\text{up}}$ and $v^{\kappa+1}_{N+1/2}A^{\kappa}_{N+1/2} = Q^{\kappa+1}_{\text{down}}$, respectively. Inside the domain, the water depth and thus the wetted area at $i \pm 1/2$ can be computed from the mean value of the neighboring section centers. Casulli (1990) proposes the finite difference approximation of (5b) as

$$\frac{v^{\kappa+1}_{i+1/2} - v^{\kappa}_{i+1/2}}{\Delta t} + g\left(\partial_x h^{\kappa+1} - S_0 + n_M^2 \frac{v^{\kappa+1}_{i+1/2}|v^{\kappa}_{i+1/2}|}{R(h^{\kappa}_{i+1/2})^{4/3}}\right) + v^{\kappa}_{i+1/2}\partial_x v^{\kappa} = 0, \qquad i \in \{1 \dots N-1\}, \quad (7)$$

which can be rearranged to

$$v^{\kappa+1}_{i+1/2} = \underbrace{\frac{v^{\kappa}_{i+1/2} - \Delta t\left(v^{\kappa}_{i+1/2}\partial_x v^{\kappa} - gS_0\right)}{\alpha^{\kappa}_{i+1/2}}}_{F(v^{\kappa}_{i+1/2})} - \frac{\Delta t g}{\alpha^{\kappa}_{i+1/2}}\partial_x h^{\kappa+1}, \qquad i \in \{1 \dots N-1\}, \quad (8)$$

with $\alpha^{\kappa}_{i+1/2} = 1 + g n_M^2 |v^{\kappa}_{i+1/2}| / R(h^{\kappa}_{i+1/2})^{4/3}$. Again the first and last entry of $\boldsymbol{v}$ can be obtained from the boundary conditions. It can be seen, that this approach allows the explicit calculation of the velocity at time step $\kappa + 1$, if the water depth at that time is known. To compute the spatial derivatives of the water depth the finite difference scheme $\partial_x h^{\kappa+1}|_{x=i+1/2} = (h^{\kappa+1}_{i+1} - h^{\kappa+1}_{i})/\Delta x$ is used, while the term $v^{\kappa}_{i+1/2}\partial_x v^{\kappa}$ can be approximated using the upwind scheme

$$v^{\kappa}_{i+1/2}\partial_x v^{\kappa} = \begin{cases} v^{\kappa}_{i+1/2}\dfrac{v^{\kappa}_{i+1/2} - v^{\kappa}_{i-1/2}}{\Delta x} & v^{\kappa}_{i+1/2} \geq 0 \\ v^{\kappa}_{i+1/2}\dfrac{v^{\kappa}_{i+3/2} - v^{\kappa}_{i+1/2}}{\Delta x} & v^{\kappa}_{i+1/2} < 0. \end{cases} \quad (9)$$

After inserting (8), (6) can be reformulated as

$$(\partial_h A)^{\kappa}_i h^{\kappa}_i + \frac{\Delta t}{\Delta x}\left(F(v^{\kappa}_{i-1/2})A^{\kappa}_{i-1/2} - F(v^{\kappa}_{i+1/2})A^{\kappa}_{i+1/2}\right) = \left((\partial_h A)^{\kappa}_i + \gamma^{\kappa}_{i+1/2} + \gamma^{\kappa}_{i-1/2}\right)h^{\kappa+1}_i - \gamma^{\kappa}_{i+1/2}h^{\kappa+1}_{i+1} - \gamma^{\kappa}_{i-1/2}h^{\kappa+1}_{i-1}, \qquad i \in \{2 \dots N-1\} \quad (10)$$

with $\gamma^{\kappa}_{i\pm1/2} = \Delta t^2 g A^{\kappa}_{i\pm1/2}/(\alpha^{\kappa}_{i\pm1/2}\Delta x^2)$. Thus a tridiagonal system of linear equations can be recognized and solved using matrix inversion or the Thomas algorithm. The implicit solution of the water depth at the next time step is used within (8) to determine the velocities $\boldsymbol{v}^{n+1}$ explicitly.

3. DATA-DRIVEN SYSTEM IDENTIFICATION

Based on real measurements or simulations, data can be collected and used to identify the dynamical system. For this purpose, the data is analyzed for characteristic properties and how these properties evolve over time. This task is closely related to the Koopman theory, where a set of measurement functions, which are called observables can be identified and propagated in time using the linear Koopman operator. When first presenting the Koopman theory in (Koopman, 1931), only autonomous systems have been addressed. In recent years Proctor et al. (2016b) have extended this approaches to systems with control inputs. Generally, the observables and the corresponding Koopman operator are infinite-dimensional, but are reduced to a n-dimensional set by spatial discretisation of the original system during measurement or simulation. After spatial discretisation a nonlinear discrete-time system of the form

$$\boldsymbol{\xi}^{\kappa+1} = \boldsymbol{f}(\boldsymbol{\xi}^{\kappa}, \boldsymbol{u}^{\kappa}) \quad (11)$$

with $\boldsymbol{f}\colon \mathbb{R}^n \times \mathbb{R}^l \to \mathbb{R}^n$, the states $\boldsymbol{\xi}^{\kappa} \in \mathbb{R}^n$ and inputs $\boldsymbol{u}^{\kappa} \in \mathbb{R}^l$ is given. Regarding the St. Venant equations and the numerical scheme presented in Section 2, the state and input vector read $\boldsymbol{\xi}^{\kappa} = \left[(\boldsymbol{h}^{\kappa})^T, (\boldsymbol{v}^{\kappa})^T\right]^T$ and $\boldsymbol{u}^{\kappa} = \left[Q^{\kappa}_{\text{up}}, Q^{\kappa}_{\text{down}}\right]^T$, respectively. It can be propagated in time using (10) and (8), which is represented by the function $\boldsymbol{f}$. First the states and inputs are lifted to the state observables $\boldsymbol{\chi}^{\kappa} \in \mathbb{R}^{n_o}$ and input observables $\boldsymbol{\nu}^{\kappa} \in \mathbb{R}^l$ using

$$\boldsymbol{\chi}^{\kappa} = \boldsymbol{\psi}(\boldsymbol{\xi}^{\kappa}), \quad (12a)$$

$$\boldsymbol{\nu}^{\kappa} = \boldsymbol{\psi}_u(\boldsymbol{u}^{\kappa}), \quad (12b)$$

with the nonlinear lifting functions $\boldsymbol{\psi}\colon \mathbb{R}^n \to \mathbb{R}^{n_o}$ and $\boldsymbol{\psi}_u\colon \mathbb{R}^l \to \mathbb{R}^l$. More details on the state and input lifting for the examined problem are shown in Section 4. Thereupon aiming to identify a few but essential Koopman modes $\boldsymbol{z}^{\kappa} \in \mathbb{R}^r$, $r \ll n$ a suitable coordinate transformation $\boldsymbol{z}^{\kappa} = \boldsymbol{\varphi}(\boldsymbol{\chi}^{\kappa})$, with $\boldsymbol{\varphi}\colon \mathbb{R}^{n_o} \to \mathbb{R}^r$ has to be found. These identified Koopman modes represent a low-dimensional subspace of the lifted space and can be propagated in time using the linear time invariant system

$$\boldsymbol{z}^{\kappa+1} = \tilde{A}\boldsymbol{z}^{\kappa} + \tilde{B}\boldsymbol{\nu}^{\kappa} =: \mathcal{F}(\boldsymbol{z}^{\kappa}, \boldsymbol{\nu}^{\kappa}). \quad (13)$$

with $\tilde{A} \in \mathbb{R}^{r\times r}$ and $\tilde{B} \in \mathbb{R}^{r\times l}$. Hence, (13) can be used to approximate simulation of (11), while the original states can be approximately reconstructed using inverse transformations

$$\boldsymbol{\xi}^{\kappa} \approx \boldsymbol{\psi}^{-1}(\boldsymbol{\varphi}^{-1}(\boldsymbol{z}^{\kappa})). \quad (14)$$

In practice different approaches are used to identify suitable coordinate transformations, essential Koopman modes and how they evolve in time. Data-based methods such as DMD with control or system identification using AEs are commonly used for this purpose and will be briefly presented next.

3.1 Extended Dynamic Mode Decomposition with control

Extended Dynamic Mode Decomposition with control (EDMDc) presented by Korda and Mezić (2018) is the combination of extended DMD (Matthew O. Williams, 2015) and DMDc (Proctor et al., 2016a). It aims to determine a control-oriented ROM based on a dictionary of observables instead of using the states only. Thus a low-dimensional linear system of the form (13) can be identified and used for prediction purposes. As a database for this approach snapshots of the states and input are collected and subsequently lifted to the state and input observables using the lifting function (12a) and (12b), respectively. In contrast to the work of Korda and Mezić (2018), the inputs are also lifted here. The lifted snapshots are stored columnwise in

$$X_{\text{lift}} = \left[\boldsymbol{\chi}^0 \ \boldsymbol{\chi}^1 \ \dots \ \boldsymbol{\chi}^{m-1}\right], \quad X'_{\text{lift}} = \left[\boldsymbol{\chi}^1 \ \boldsymbol{\chi}^2 \ \dots \ \boldsymbol{\chi}^{m}\right],$$
$$\mathcal{U}_{\text{lift}} = \left[\boldsymbol{\nu}^0 \ \boldsymbol{\nu}^1 \ \dots \ \boldsymbol{\nu}^{m-1}\right],$$

where the i-th column of the X'_{lift} matrix should be obtained from the corresponding column of the states in X_{lift} and inputs from $\mathcal{U}_{\text{lift}}$. Within EDMDc, this propagation is approximated by a linear dynamical model written as

$$X'_{\text{lift}} = AX_{\text{lift}} + B\mathcal{U}_{\text{lift}} = [A \ B]\begin{bmatrix} X_{\text{lift}} \\ \mathcal{U}_{\text{lift}} \end{bmatrix} = G\Omega. \quad (15)$$

The unknown matrices $A \in \mathbb{R}^{n_o \times n_o}$ and $B \in \mathbb{R}^{n_o \times l}$ are determined by minimizing the one-step linear prediction error of the observable snapshot matrices. Therefore the singular value decomposition (SVD) of the stacked matrix $\Omega \approx \tilde{U}\tilde{\Sigma}\tilde{V}^*$ has to be computed. By unstacking the (truncated) matrix of left-singular vectors as $\tilde{U} = \begin{bmatrix}\tilde{U}_A \; \tilde{U}_B\end{bmatrix}^T$ the system matrices can be approximated using

$$[A \; B] \approx \begin{bmatrix}\bar{A} \; \bar{B}\end{bmatrix} = \begin{bmatrix}X'_{\text{lift}}\tilde{V}\tilde{\Sigma}^{-1}\tilde{U}_A^* \; X'_{\text{lift}}\tilde{V}\tilde{\Sigma}^{-1}\tilde{U}_B^*\end{bmatrix}. \quad (16)$$

Thereupon to obtain a ROM in the form of (13) the coordinate transformation

$$\boldsymbol{\chi}^\kappa = \hat{U}\boldsymbol{z}^\kappa =: \boldsymbol{\varphi}_{\text{DMD}}^{-1}(\boldsymbol{z}^\kappa) \quad (17)$$

is applied, where $\hat{U} \in \mathbb{R}^{n_o \times r}$ contains the left-singular vectors corresponding to the first r dominant singular values. $\hat{U}$ can be obtained from the SVD of the matrix X'_{lift} and its subsequent truncation. Finally the ROM system and input matrices from (13) are given by

$$\begin{aligned}\tilde{A} &= \hat{U}^*\bar{A}\hat{U},\\ \tilde{B} &= \hat{U}^*\bar{B},\end{aligned} \quad (18)$$

which are purely derived from the snapshot matrices of the observables. Further details are given in Korda and Mezić (2018); Proctor et al. (2016a).

3.2 System identification using autoencoders

An alternative approach is to use (deep) neuronal networks for Koopman operator identification. Applications to nonlinear systems and PDEs have been presented by Lusch et al. (2018) and Gin et al. (2021), respectively. Basically, AEs consist of an encoder and a decoder part, which can be used to compress the input at the encoder $\boldsymbol{\varphi}_{\text{AE}}(\boldsymbol{\chi}^\kappa)$ to a reduced order state $\boldsymbol{z}^\kappa$ of dimension r. The projection of the encoder from $\boldsymbol{\chi}^\kappa$ to $\boldsymbol{z}^\kappa$ can be seen as a nonlinear coordinate transformation. Again the ROM state can be propagated in time using (13) with less computational effort. As a counterpart to the encoder, the decoder $\boldsymbol{\varphi}_{\text{AE}}^{-1}$ can be used to map the reduced state back to the observables, which then can be transformed to the discretized states. The AE scheme for identification of an appropriate coordinate transformation and the corresponding dynamical system is shown schematically in Figure 3. For the sake of clarity, however, only the one-step propagation of the state $\boldsymbol{z}^\kappa$ is shown. The propagation can also take place for several time steps before the decoder is applied. Thus an q-step prediction of the low-dimensional state can be used to obtain the observables after q time steps.

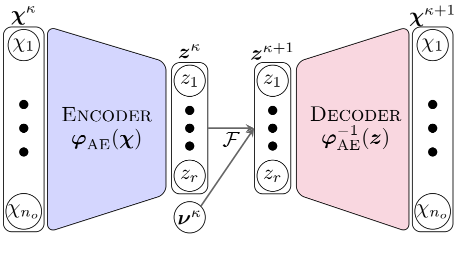
$\boldsymbol{\chi}^\kappa$
χ_1
χ_{n_o}
ENCODER
$\boldsymbol{\varphi}_{\text{AE}}(\boldsymbol{\chi})$
$\boldsymbol{z}^\kappa$
z_1
z_r
$\mathcal{F}$
$\boldsymbol{\nu}^\kappa$
$\boldsymbol{z}^{\kappa+1}$
z_1
z_r
DECODER
$\boldsymbol{\varphi}_{\text{AE}}^{-1}(\boldsymbol{z})$
$\boldsymbol{\chi}^{\kappa+1}$
χ_1
χ_{n_o}

Fig. 3. Model order reduction scheme using autoencoder.

To fit the encoder and decoder to the training data, a parameter optimization has to be carried out based on an underlying loss function. Thereby three main parts have to be considered. First the AE should accurately reconstruct the original observables after encoding and decoding. The corresponding part of the loss function reads

$$l_1 = \left\| \boldsymbol{\chi}^\kappa - \varphi_{\text{AE}}^{-1}(\varphi_{\text{AE}}(\boldsymbol{\chi}^\kappa)) \right\|_{L_2}. \quad (19)$$

Secondly, the i-th step propagation of the encoded state of $\boldsymbol{\chi}^\kappa$ should be identical to the encoded state at time step $\kappa + i$. In the loss function q steps will be considered. Thus the second part of the loss function can be formulated as

$$l_2 = \sum_{i=1}^{q} \left\| \varphi_{\text{AE}}(\boldsymbol{\chi}^{\kappa+i}) - \mathcal{F}^i(\varphi_{\text{AE}}(\boldsymbol{\chi}^\kappa), \boldsymbol{\nu}^+) \right\|_{L_2} \quad (20)$$

with

$$\mathcal{F}^i(\varphi_{\text{AE}}(\boldsymbol{\chi}^\kappa), \boldsymbol{\nu}^+) = \mathcal{F}(...(\mathcal{F}(\varphi_{\text{AE}}(\boldsymbol{\chi}^\kappa, \boldsymbol{\nu}^\kappa)...), \boldsymbol{\nu}^{\kappa+i-1}), \quad (21)$$

which denotes the recursive use of (13). Additionally the decoded i-th step prediction should be close to the original observables at time $\kappa + i$. Hence the third part

$$l_3 = \sum_{i=1}^{q} \left\| \boldsymbol{\chi}^{\kappa+i} - \varphi_{\text{AE}}^{-1}(\mathcal{F}^i(\varphi_{\text{AE}}(\boldsymbol{\chi}^\kappa), \boldsymbol{\nu}^+)) \right\|_{L_2} \quad (22)$$

is added to the loss function, so that the weighted multi-objective loss function $l = l_1 + w_\alpha l_2 + w_\beta l_3$ can be used to train the AE for the identification of the linear ROM and the appropriate coordinate transformations.

One advantage of AEs compared to EDMDc is that nonlinear transformations can be used to obtain the reduced order space. But the drawback compared to EDMDc is that the number of ROM states has to be set a priori when constructing the neuronal network, i.e., before potential modes are identified. In addition, the effort required to implement EDMDc is significantly lower.

4. PROCESS-INSIGHT-BASED STATE LIFTING

Before applying EDMDc and AE to obtain a ROM for an open channel and for fluids in general, special attention has to be paid to mass conservation. Both MOR approaches from Section 3 do not satisfy conservation of the total channel volume. To tackle this issue the snapshots can be corrected using process information about the normal depth and discharge, which is denoted by the lifting (12). Chen et al. (2012) presented a scheme, where a base flow is computed from the mean value and subsequently subtracted from the state snapshots to obtain the observables. In this work, however, the knowledge about the underlying system is used to lift the states. Therefore the total volume of the channel has to be computed for each snapshot using

$$V^\kappa = \sum_{i=1}^{N} A(h_i^\kappa)\Delta x \quad (23)$$

with $A(h_i)$ from (3). The normal depth

$$h_n^\kappa = -\frac{B}{2m} + \sqrt{\left(\frac{B}{2m}\right)^2 + \frac{V^\kappa}{Lm}} =: h_n(V^\kappa) \quad (24)$$

can be obtained from the inversion of (23) combined with (3). In addition to the corrected water depth, the corrected discharge, which is motivated by the boundary condition is considered within the observables. Therefore the normal discharge can be computed from (24) and is given by

$$Q_n^\kappa = \frac{A(h_n^\kappa)R^{2/3}(h_n^\kappa)\sqrt{S_0}}{n} \quad (25)$$

Thus the discrete states $\boldsymbol{\xi}^\kappa$ and inputs $\boldsymbol{u}^\kappa$ can be lifted to the state and input observables using

$$\boldsymbol{\chi}^\kappa = \left[(\boldsymbol{h}^\kappa - \boldsymbol{h}_n^\kappa)^T, (\boldsymbol{v}^\kappa \boldsymbol{A}^\kappa - \boldsymbol{Q}_n^\kappa)^T\right]^T, \quad (26)$$

$$\boldsymbol{\nu}^\kappa = \boldsymbol{u}^\kappa - [Q_n^\kappa, Q_n^\kappa]^T, \quad (27)$$

respectively. Thereby $\boldsymbol{h}_n^\kappa = \mathbf{1}_N h_n^\kappa$ and $\boldsymbol{Q}_n^\kappa = \mathbf{1}_{N+1} Q_n^\kappa$ holds, while $\boldsymbol{A}^\kappa$ contains the wetted area on the cell edges, which as in Section 2, are determined from the water depths h_i^κ. In order to reconstruct the spatially discretized states from the ROM states, first $\boldsymbol{\varphi}^{-1}$ has to be used to obtain the reconstructed observables. Afterwards the inverse lifting has to be applied. Therefore the total channel volume is computed using the mass balance

$$\dot{V} = Q_{\mathrm{up}} - Q_{\mathrm{down}}, \qquad V_0 = V(0). \quad (28)$$

Again the normal depth and normal discharge can be obtained from (28) using (24) and (25), respectively. These quantities have to be added to the reconstructed observables to obtain the water depth and the discharge. Additionally the velocity can be computed by using (4). The ROM is therefore left with the task of describing deviations around the normal depth, while the total volume is calculated separately. In this way, the volume and thus the total mass of the channel is preserved.

5. APPLICATION TO THE ST. VENANT EQUATIONS

For the evaluation of the MOR techniques an open channel with trapezoidal profile is chosen. The used parameters are listed in Appendix A. After numerical simulation of the St. Venant equations using (10) and (8), with $N = 100$ the observables are determined from the scheme presented in Section 4. Thus a wide database has been created from several simulations with transitions between non-uniform flow regimes, white noise and waveform actuations. The computation of the EDMDc and AE scheme has been done in Matlab and TensorFlow, respectively. The activation functions of the autoencoder layers are chosen to be sigmoid functions.

First the coordinate transformation and the simulative behavior of the ROM are reviewed depending on the ROM dimension. Therefore the directly reconstructed observables $\boldsymbol{\chi}_{EDMDc}^{ROM} = \hat{U}\hat{U}^*\boldsymbol{\chi}$ for EDMDc and $\boldsymbol{\chi}_{AE}^{ROM} = \boldsymbol{\varphi}_{AE}^{-1}(\boldsymbol{\varphi}_{AE}(\boldsymbol{\chi}))$ for AE are compared to the original observables $\boldsymbol{\chi}$. Afterwards the simulation accuracy of the identified ROM is evaluated by computing future observables using the ROM. For this purpose an initial ROM state has to be computed from the coordinate transformation. Starting from this state, future ROM states and thus future observables can be reconstructed using $\boldsymbol{\varphi}^{-1}$, which are compared to the numerical solution and the subsequent lifting. Both quantities are considered separately and evaluated using the L_2 error norm, which exemplary reads

$$\left\| \boldsymbol{h} - \boldsymbol{h}^{ROM} \right\|_{L_2} = \sqrt{\sum_{i=1}^{N} |h_i - h_i^{ROM}|^2} \quad (29)$$

for the water depth. Figure 4 shows the average L_2 error norm, depending on the dimension of the ROM, for 50 validation scenarios. Thereby the case of zero modes represents the scenario, where only the normal depth and discharge are used to approximate the dynamic behavior of the system. The quality of direct reconstruction is shown in top part. It can be seen that the accuracy increases with the number of modes, whereby a change at lower mode numbers results in a more significant impact than the same increase at higher mode numbers. This can be particularly seen in the reconstruction of the water depth, where two modes provide approximately the same accuracy as 15 modes. Both the reconstruction error of the water depth and the discharge are smaller when using EDMDc compared to the AE approach. A similar behavior can be observed for the L_2 error norm of the reconstructed observables from the ROM simulations with a simulation horizon of 1.5 h, which is shown in Figure 4 (bottom). Additionally, it can be seen that the L_2 error norm of the water depth is almost unchanged for the simulation and subsequent reconstruction compared to reconstruction alone. For EDMDc the L_2 error norm of the discharge decreases until 8 modes and then starts to slightly increase, which can be attributed to the fact that some modes which represent more detailed structures of the training data are considered there. These structures are not necessarily included in the validation data and thus lead to weaker results. Regarding the AE scheme, peaks at 3 and 12 modes can be observed. Even though the accuracy there is lower than without using a MOR approach, it shows a lower reliability of this approach compared to EDMDc.

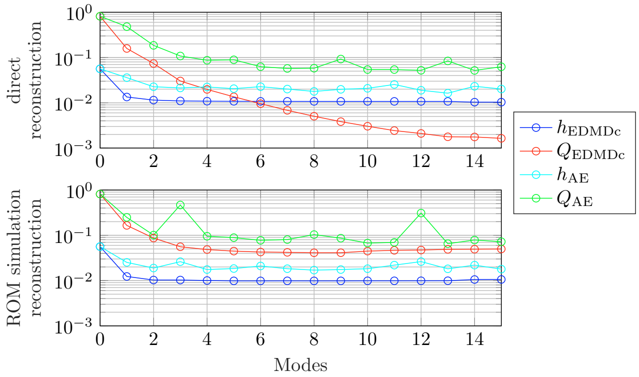

Fig. 4. L_2 error norm of the MOR schemes compared to the discrete solution of the St. Venant equations, with direct (top) and ROM simulation (bottom) reconstruction.

The number of modes should be chosen based on the required accuracy and available computational resources. For water networks, the reduction to a minimum number seems attractive to reduce the computational effort. To give a rough estimate of the computational times, the duration of all training scenarios was recorded. This shows that the ROM of the form (13) can be run within under 0.1% of the time compared to the solution of the St. Venant equation using (10) and (8). When the discretized states should be reconstructed from the ROM states using (14), the calculation time slightly increases, but is still less than 1% compared to the numerical solution. Based on this analysis and the results from Fig. 4 the choice of $r = 6$ modes seems appropriate for state reconstruction including simulations and will be used subsequently.

For a more detailed analysis of the dynamic behavior, a scenario with the boundary excitation shown in Fig. 6 is used. This excitation is not included in the training set.

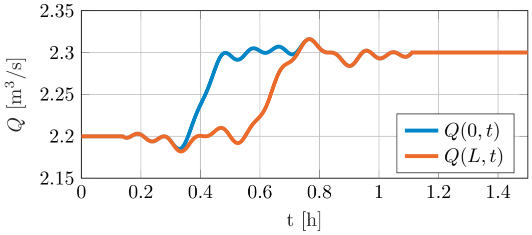

Fig. 6. System input for ROM evaluation.

The reconstructed states, i.e., the water depth and velocity of the ROM simulation with this boundary excitation can be seen in Fig. 5. Both, EDMDc and the AE approach are able to replicate the quantitative behavior of the water in the open channel. Starting at the uniform flow with a constant discharge of $Q(L,t) = Q(0,t) = Q_n$, the EDMDc approach ideally reproduces both initial states, while the AE approach shows small deviations. The rise of the left and right boundary discharge cause a slow change of the water surface and the velocity profile towards the non-uniform flow regime with a constant flow $Q > Q_n$. During this rise first the water depth increases at the left bound of the domain, followed by the decrease at the right bound of the domain. When looking at Fig. 5 it can be seen, that this behavior is replicated by both MOR approaches, with EDMDc giving slightly better results. A more significant difference occurs at the fluid velocity. In contrast to the discrete simulation of the velocity where waves can be observed, a closer look at the results of both approaches shows that these waves appear washed out. Again, this effect is less noticeable when using EDMDc. This can also be seen from the L_2 error norm shown in Fig. 7. There it is also visible that after the transition to the non-uniform flow regime, a constant L_2 error norm occurs, which indicates a steady-state solution of the ROM.

Overall, the surface and velocity profile of the water within the channel can be reconstructed with small deviations using only a few modes, six in this example. Due to the introduced preprocessing, the total volume of the fluid is preserved, so that the water depth can be approximated during the waveform actuation and in the non-uniform flow case, which is given after 1.5 hours.

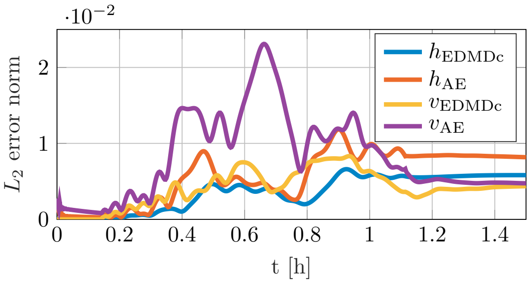

Fig. 7. L_2 error norm of the ROM simulations (Fig. 5, middle/right) compared to the discrete solution of the St. Venant equations (Fig. 5, left).

6. CONCLUSION

Data-driven Koopman operator identification using extended Dynamic Mode Decomposition with control and autoencoders applied to the St. Venant equations has been presented. After process-insight-based state lifting a suitable coordinate transformation and a control-oriented, linear ROM can be identified and subsequently used for efficient simulation under consideration of mass conservation. Both approaches reproduce the original states quantitatively well, with EDMDc giving slightly better results. Additionally, this method can be applied with significantly less effort. However, as with all data-driven applications, it should be noted that the training data sets, the range of the EDMD dictionary and the structure of the AE have a crucial impact on the accuracy of the ROM. Overall, the ability to efficiently simulate the dynamic behavior of both the water depth and discharge for the whole channel is a big advantage compared to other approximative models.

As this work is a first step towards simulation and control of water networks based on Koopman theory, further improvement on reduced order modeling of a single channel will be addressed in the future. Therefore methods presented by Maulik et al. (2021); Lu and Tartakovsky (2020), which seem promising when applied to advection-dominant problems, could be used. Since these methods have difficulties to handle multiwaves, an extension has to be found, which can then be tested on the St. Venant equations. Additionally a wider range of dictionary functions applied to the lifted observables could be used for further improvement of EDMDc and AE performance. Since the presented approach has proven to be efficient and accurate for open channel simulation, it can be further coupled with the hydrodynamic simulation software SWMM and used as an underlying model for model-based optimal control.

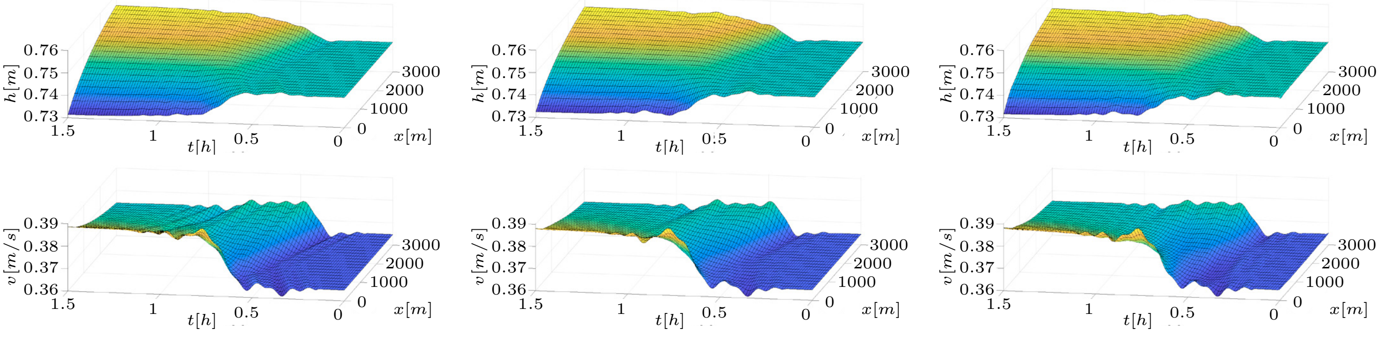

Fig. 5. Water depth (top row) and discharge (bottom row) simulation of an open channel using the discretized (left column), EDMDc (middle column) and autoencoder (right column) model.

ACKNOWLEDGEMENTS

In addition to the financial support by Interreg Deutschland-Danmark through the NEPTUN project, the authors thank LNH water for fruitful discussions on hydrodynamic modeling and the Stormwater Management Model.

REFERENCES

Ahmed, S., San, O., Bistrian, D., and Navon, I. (2020). Sampling and resolution characteristics in reduced order models of shallow water equations: Intrusive vs nonintrusive. *International Journal for Numerical Methods in Fluids*, 92. doi:10.1002/fld.4815.

Arbabi, H., Korda, M., and Mezić, I. (2018). A data-driven koopman model predictive control framework for nonlinear partial differential equations. In *2018 IEEE Conference on Decision and Control (CDC)*, 6409–6414. doi:10.1109/CDC.2018.8619720.

Benkhaldoun, F. and Seaïd, M. (2010). A simple finite volume method for the shallow water equations. *Journal of Computational and Applied Mathematics*, 234(1), 58–72. doi:https://doi.org/10.1016/j.cam.2009.12.005.

Bistrian, D. and Navon, I. (2015). An improved algorithm for the shallow water equations model reduction: Dynamic Mode Decomposition vs POD. *International Journal for Numerical Methods in Fluids*, 78, 552–580. doi:10.1002/fld.4029.

Brunton, S.L., Budišić, M., Kaiser, E., and Kutz, J.N. (2021). Modern Koopman Theory for Dynamical Systems.

Brunton, S.L. and Kutz, J.N. (2019). *Data-Driven Science and Engineering: Machine Learning, Dynamical Systems, and Control*. Cambridge University Press. doi:10.1017/9781108380690.

Casulli, V. (1990). Semi-implicit finite difference methods for the two-dimensional shallow water equation. *Journal of Computational Physics*, 86, 56–74.

Chen, K.K., Tu, J.H., and Rowley, C.W. (2012). Variants of dynamic mode decomposition: Boundary condition, koopman, and fourier analyses. *Journal of Nonlinear Science*, 22, 887–915.

Conde, G., Quijano, N., and Ocampo-Martinez, C. (2021). Modeling and control in open-channel irrigation systems: A review. *Annual Reviews in Control*, 51. doi:10.1016/j.arcontrol.2021.01.003.

Diagne, A., Diagne, M., Tang, S., and Krstic, M. (2015). Backstepping stabilization of the linearized Saint-Venant-Exner Model: Part I - state feedback. In *2015 54th IEEE Conference on Decision and Control (CDC)*, 1242–1247. doi:10.1109/CDC.2015.7402381.

Gin, C., Lusch, B., Brunton, S.L., and Kutz, J.N. (2021). Deep learning models for global coordinate transformations that linearise PDEs. *European Journal of Applied Mathematics*, 32(3), 515–539. doi:10.1017/S0956792520000327.

Koopman, B.O. (1931). Hamiltonian Systems and Transformation in Hilbert Space. *Proceedings of the National Academy of Sciences*, 17(5), 315–318. doi:10.1073/pnas.17.5.315.

Korda, M. and Mezić, I. (2018). Linear predictors for nonlinear dynamical systems: Koopman operator meets model predictive control.

Lu, H. and Tartakovsky, D.M. (2020). Lagrangian dynamic mode decomposition for construction of reduced-order models of advection-dominated phenomena. *Journal of Computational Physics*, 407, 109229. doi:https://doi.org/10.1016/j.jcp.2020.109229.

Lusch, B., Kutz, J., and Brunton, S. (2018). Deep learning for universal linear embeddings of nonlinear dynamics. *Nature Communications*, 9. doi:10.1038/s41467-018-07210-0.

Maksakov, A. and Palis, S. (2021). Koopman-based data-driven control for continuous fluidized bed spray granulation with screen-mill-cycle. *Journal of Process Control*, 103, 48–54. doi:https://doi.org/10.1016/j.jprocont.2021.05.006.

Matthew O. Williams, Ioannis G. Kevrekidis, C.W.R. (2015). A Data–Driven Approximation of the Koopman Operator: Extending Dynamic Mode Decomposition. *Journal of Nonlinear Science*, 25(1), 1307–1346. doi:10.1007/s00332-015-9258-5.

Maulik, R., Lusch, B., and Balaprakash, P. (2021). Reduced-order modeling of advection-dominated systems with recurrent neural networks and convolutional autoencoders. *Physics of Fluids*, 33(3), 037106. doi:10.1063/5.0039986.

Proctor, J.L., Brunton, S.L., and Kutz, J.N. (2016a). Dynamic Mode Decomposition with Control. *SIAM J. Appl. Dyn. Syst.*, 15, 142–161.

Proctor, J.L., Brunton, S.L., and Kutz, J.N. (2016b). Generalizing Koopman Theory to allow for inputs and control.

Rabbani, T., Di Meglio, F., Litrico, X., and Bayen, A. (2010). Feed-Forward Control of Open Channel Flow Using Differential Flatness. *Control Systems Technology, IEEE Transactions on*, 18, 213 – 221. doi:10.1109/TCST.2009.2014640.

Saint-Venant, A.B.d. (1871). Théorie du mouvement non permanent des eaux, avec application aux crues des rivières et a l'introduction de marées dans leurs lits. *Comptes Rendus de l'Académie des Sciences*, 73, 147–154 and 237–240.

Utnes, T. (1990). A finite element solution of the shallow-water wave equations. *Applied Mathematical Modelling*, 14(1), 20–29. doi:https://doi.org/10.1016/0307-904X(90)90159-3.

Xu, M., Negenborn, R., Overloop, P., and van de Giesen, N. (2012). De Saint-Venant equations-based model assessment in model predictive control of open channel flow. *Advances in Water Resources*, 49, 37–45. doi:10.1016/j.advwatres.2012.07.004.

Zeng, N., Cen, L., Xie, Y., and Zhang, S. (2020). Nonlinear optimal control of cascaded irrigation canals with conservation law PDEs. *Control Engineering Practice*, 100, 104407. doi:10.1016/j.conengprac.2020.104407.

Appendix A. USED PARAMETERS

		Channel		
L	B	n_M	m	S_0
3000	7	0.02	1.5	$1 \cdot 10^{-4}$

Autoencoder layers		loss weighting	
Encoder	Decoder	w_α	w_β
[120, 60, 30]	[30, 60, 120]	50	$1 \cdot 10^3$